THE PENNSYLVANIA STATE UNIVERSITY
SCHREYER HONORS COLLEGE

DEPARTMENT OF ASTRONOMY AND ASTROPHYSICS

A REAL PIECE OF SKY: CHROMATIC ATMOSPHERIC EFFECTS AND THE NEID SPECTROGRAPH

LENNON NICHOL
SPRING 2026

A thesis
submitted in partial fulfillment
of the requirements
for baccalaureate degree
in Astronomy and Astrophysics
with honors in Astronomy and Astrophysics

Reviewed and approved* by the following:

Jason T. Wright
Professor of Astronomy and Astrophysics
Thesis Supervisor

Cindy Yuexing Gulis
Associate Professor of Astronomy and Astrophysics
Honors Adviser

*Signatures are on file in the Schreyer Honors College.

Abstract

Operating on the WIYN 3.5m telescope at Kitt Peak National Observatory, NEID is a high-resolution spectrograph designed to achieve sub-meter-per-second radial velocity precision, enabling the detection and characterization of exoplanet masses around nearby stars. The chromatic exposure meter delivers precise flux-weighted midpoint times and their corresponding barycentric corrections (BCs) as a function of wavelength, to account for variations from atmospheric dispersion. These corrections are automatically computed using NEID's exposure meter flux/time data, incorporating variations in atmospheric transparency and photon statistics. We have independently validated the values reported by the NEID data reduction pipeline, and are quantifying the contribution of BC uncertainty to the overall NEID RV error budget. Furthermore, we characterize how the magnitude and functional form of the variation of BCs varies with wavelength, and validate the necessity of chromatic exposure meters on EPRV instruments like NEID.

Table of Contents

List of Figures iii

List of Tables iv

Acknowledgments v

1 Introduction 1
- 1.1 A Means of Garnering Radial Velocities 2
- 1.2 The Importance of the Barycentric Correction 3
- 1.3 Application to NEID and Our Present Analysis 4

2 Methodology and Results 5
- 2.1 Chromatic Barycentric Correction Pipeline 6
  - 2.1.1 FITS-File Parsing and the Open-Shutter Interval 6
  - 2.1.2 Exposure Timing Verification and Correction 6
  - 2.1.3 Geometric and Flux-Weighted Midpoint Times 7
  - 2.1.4 Barycentric Velocity Calculation with `barycorrpy` 8
  - 2.1.5 Polynomial Modeling of Chromatic Dependence 9
  - 2.1.6 Residual Analysis and Goodness-of-Fit Metrics 11
  - 2.1.7 Exposure-Level Summary Statistics 12
  - 2.1.8 Multi-Exposure Comparison and Identification of Extreme Cases 12

3 Conclusion 15
- 3.1 The Analysis So Far 16
  - 3.1.1 Discussion 16
  - 3.1.2 Future Work 16

Bibliography 18

List of Figures

2.1 An Example Tau Ceti Exposure 10
2.2 An Example Sigma Draconis Exposure 10
2.3 Curiouser and Curiouser: An Exceedingly Well-Fit Polynomial 11
2.4 Tau Ceti: Two Extreme Exposures 13
2.5 Sigma Draconis: Two Extreme Exposures 13

List of Tables

1.1 Measured RV Amplitudes of Confirmed Exoplanets 3
2.1 Astrometric Parameters for HD 10700 8

Acknowledgments

First and foremost, I thank my thesis advisor, Dr. Jason T. Wright, for his unwavering guidance and insight throughout this project. His passion for exoplanetary science and precision radial velocities is utterly infectious, and I have learned an immense amount from his mentorship. Thank you for always making the time to discuss, to refine figures, and to clarify my writing. I must also thank Dr. Olivia Curtis, for helping me troubleshoot code and for providing extensive insight into refining my approach again and again. This work would simply not have been possible without the two of you.

I am grateful to The Pennsylvania State University and the Department of Astronomy and Astrophysics for supplying the resources and the community that made this research possible. The Schreyer Honors College has been a constant source of encouragement throughout my undergraduate career, and I thank them for fostering a culture of academic excellence.

I extend my sincerest thanks to the NEID science team, whose collective effort built and operates the incredible instrument that provided the data for this thesis. The exposure meter at the heart of this work is a testament to the team's dedication to pushing the frontier of EPRV work.

To my mom, dad, and Ace: thank you for a lifetime of support, for always believing in me, and for fostering my curiosity about the universe from a young age. Your sacrifices have made every step of this journey possible.

To my grandma and grandpa: thank you for your love, your wisdom, and your constant encouragement. You have always been my champions, and I hope this work makes you proud.

Finally, to my partner, Maggie: thank you for your endless understanding, especially during the late nights and long weekends spent writing and coding. Somewhere in the cosmos, amid the billions of galaxies and trillions of stars, we found each other. You make this vastness feel like home.

This thesis is for all of you.

Chapter 1

Introduction

1.1 A Means of Garnering Radial Velocities

Since the discovery of 51 Pegasi B in 1995 [1], hundreds of extrasolar worlds have been detected and characterized via the radial velocity method. But the underlying physical basis of the radial velocity method is a delicate dance: a planet and its host star do not move as a singular body orbiting some static central mass. Instead, both bodies orbit a common center of mass, the barycenter of the system. The star, however, is considerably more massive than the planetary companion resulting in a shrunken orbit around the barycenter—but it is not nil. As the star wobbles towards and away from the observer its spectrum is Doppler shifted. Measuring these periodic wavelength shifts allows the line-of-sight component of the star's motion to be inferred, and from that motion one may constrain the existence and properties of that unseen companion, namely the mass.

We start our derivation with the classic two-body problem [2]. For a star of mass $M_\star$ and a planet of mass M_p, separated by semi-major axis a, Kepler's third law yields

$$P^2 = \frac{4\pi^2 a^3}{G(M_\star + M_p)}, \tag{1.1}$$

where P is the orbital period and G is the gravitational constant. The star and planet orbit the barycenter with semi-major axes $a_\star$ and a_p, respectively, satisfying

$$M_\star a_\star = M_p a_p, \tag{1.2}$$

so that

$$a_\star = a\frac{M_p}{M_\star + M_p}. \tag{1.3}$$

Thus, even though the planet is not directly observed, the star's barycentric orbit retains information about the planet mass and orbital geometry.

If the orbit was perfectly circular and viewed edge-on, the observed radial velocity would be just a simple sinusoid. In a more general sense, the line-of-sight velocity of the star is obtained via projecting the orbital motion onto the observer's direction. For a Keplerian orbit, the stellar radial velocity is commonly written as

$$v_r(t) = K\left[\cos\big(\omega + f(t)\big) + e\cos\omega\right] + \gamma, \tag{1.4}$$

where K is the semi-amplitude, ω is the argument of periastron, $f(t)$ is the true anomaly, e is the orbital eccentricity, and γ is the system velocity offset. K is crucial here, as it sets the characteristic size of the Doppler signal induced by the planetary body. For a circular orbit, the orbital speed of the star about the barycenter is

$$v_\star = \frac{2\pi a_\star}{P}, \tag{1.5}$$

and the observable component is reduced by i relative to the plane of the sky. For eccentric orbits, as is the most usual and common case in nature, there is an additional factor of $(1-e^2)^{-1/2}$, yielding

$$K = \left(\frac{2\pi G}{P}\right)^{1/3}\frac{M_p \sin i}{(M_\star + M_p)^{2/3}}\frac{1}{\sqrt{1-e^2}}. \tag{1.6}$$

In the common limit $M_p \ll M_\star$, this becomes

$$K \approx \left(\frac{2\pi G}{P}\right)^{1/3} \frac{M_p \sin i}{M_\star^{2/3}} \frac{1}{\sqrt{1-e^2}}. \tag{1.7}$$

And yet, this provides a most vital limitation. The amplitude can be translated into the inferred mass, $M_p \sin i$, but not M_p itself. This is because the inclination is generally unknown unless the system is also observed via transit. And so this measurable quantity is not actually the velocity, but a shift in spectral wavelength. The redshift z is defined by

$$z \equiv \frac{\lambda_{\text{meas}} - \lambda_{\text{emit}}}{\lambda_{\text{emit}}}, \tag{1.8}$$

and in the non-relativistic limit appropriate for stellar reflex motions,

$$v_r \approx cz, \tag{1.9}$$

where c is the speed of light. As Wright emphasizes, modern Doppler work is fundamentally a redshift-measurement problem rather than a direct velocity-measurement problem, and this distinction becomes increasingly important once one seeks meter-per-second and centimeter-per-second precision [3].

Extrasolar Planet	**RV Amplitude** (K)
HD 209458 b	$\sim 85 \text{ m s}^{-1}$
51 Peg b	$\sim 56 \text{ m s}^{-1}$
Gliese 581 c	$\sim 3.1 \text{ m s}^{-1}$
Proxima Cen b	$\sim 1.4 \text{ m s}^{-1}$
Earth Analog (theoretical)	$\sim 0.09 \text{ m s}^{-1}$

Table 1.1: Measured radial velocity semi-amplitudes (K) for a selection of confirmed exoplanets, compared to the theoretical Earth-twin signal. Values are from the discovery papers: HD 209458 b [4]: 51 Peg b [1]; Gliese 581 c [5]; Proxima Cen b [6]. The difficulty of achieving Earth-analog detection, $\sim 9 \text{ cm s}^{-1}$, becomes apparent when compared to even recent measurements [7].

At that level, numerous astrophysical and instrumental effects that were previously negligible become significant sources of error. These include stellar variability, contamination from the terrestrial atmosphere, and various instrumental systematics. The apparent velocity shifts caused by the Earth's motion are often orders of magnitude larger than the planetary signals of interest: the barycentric motion of the observatory can produce shifts of tens of kilometers per second, whereas Earth-like planets would induce stellar reflex motions at the level of centimeters per second.

1.2 The Importance of the Barycentric Correction

Because the Earth both rotates and orbits the Sun, the line-of-sight velocity between a telescope and the observed star varies not only over the duration of a single exposure, but between observational epochs. If left unaccounted for, this can introduce apparent shifts many orders of magnitude larger than the planetary signal one is trying to measure. Precise radial velocity studies must therefore transform measured redshifts into the barycentric reference frame in order to isolate the intrinsic motion of the star.

This transforms the redshift measured in the observatory frame to that of an observer at rest with respect to the barycenter of the solar system. At high precision, this is not simply a matter of just subtracting one velocity from another, as the redshift transformations are multiplicative.

Following [8], the measured and corrected redshifts are related by

$$z_{\mathrm{true}} = (1 + z_{\mathrm{meas}})(1 + z_B) - 1, \tag{1.10}$$

where z_{meas} is the redshift measured by the spectrograph and z_B is the barycentric correction term. This formulation is essential because a simple additive velocity subtraction neglects cross terms, growing far more important when aiming for extreme precision.

The physical origin of z_B is the motion of the observatory relative to the incoming wavefront from the star, together with additional geometric and relativistic effects. The dominant term here is the velocity of the observatory itself projected onto the instantaneous line of sight to the star. However, a complete treatment at the centimeter-per-second level must also account for the Earth's rotation and changing orientation, precession, proper motion of the star, parallax, secular acceleration, gravitational redshift terms within the solar system. But achieving $\sim 1\ \mathrm{cm\,s^{-1}}$ accuracy [8] requires not only the development of a rigorous algorithm, but also highly accurate observational inputs: observatory position, target coordinates, proper motions, parallax, and precise timing.

A common approximation is to evaluate the barycentric correction at a single representative time for the exposure, such as the midpoint time between shutter open and shutter close. While this is adequate for moderate precision work, it becomes insufficient for spectrographs attempting extremely precise radial velocity measurements.

1.3 Application to NEID and Our Present Analysis

The NEID spectrograph is a next-generation extreme-precision radial velocity instrument designed to detect and characterize exoplanets by measuring Doppler shifts in stellar spectra with high stability and precision. Like other instruments operating at the frontier of radial velocity precision, NEID must account not only for the gross motion of the Earth, but also for subtle time and wavelength dependent effects that alter the appropriate barycentric correction during an exposure. While the chromatic barycentric effect has been discussed and demonstrated in the context of other instruments, such as EXPRES, it must be examined and validated in the specific instrumental context of NEID, whose exposure meter, wavelength coverage, and observing conditions differ from those of other systems.

Changes in Earth's atmospheric transmission during an exposure can alter the flux received at different wavelengths in different ways [9, 10]. Variations in air mass, clouds, aerosols, seeing, and atmospheric water vapor affect blue and red wavelengths differently, so the temporal weighting of the detected photons becomes chromatic. Consequently, the effective observation time becomes a function of wavelength. Because the barycentric correction itself depends on time, this chromatic temporal weighting produces wavelength-dependent barycentric corrections.

Chapter 2

Methodology and Results

2.1 Chromatic Barycentric Correction Pipeline

Our analysis implements and extends the methodology established by [10] for characterizing chromatic barycentric corrections, developing a Python reduction pipeline to verify exposure timing, compute precise barycentric corrections, and quantify wavelength-dependent systematic offsets that arise when geometric and photon-weighted exposure times differ. The central purpose of the pipeline is to determine, for each exposure and for each spectral order, how much error is introduced if the barycentric correction is evaluated at a geometric midpoint time rather than at the flux-weighted midpoint time implied by the detected photons.

2.1.1 FITS-File Parsing and the Open-Shutter Interval

For each observation, the pipeline opens the FITS file and reads the primary header together with the exposure-meter data stored in HDU 14. The primary header provides the observation start time, exposure time, target coordinates, proper motions, parallax, systemic radial velocity, and observatory information. And from the exposure meter, the pipeline extracts a time series of flux as a function of both spectral order and time bin. The exposure meter provides a low spectral resolution, time-resolved record of the photon flux entering the instrument during the exposure. We also extract the wavelength solution stored in HDU 14. These wavelengths are converted from Å to nm and are later used to construct the chromatic dependence of the barycentric correction difference.

The first task is to identify the portion of the exposure during which the shutter is fully open and useful stellar flux is being recorded. To do this, the pipeline sums the exposure-meter flux over all spectral orders to define a total-flux time series. A threshold of 1000 counts is then applied to this summed flux, and only time bins with total flux above this threshold are considered to lie within the illuminated part of the exposure. The threshold is applied to the summed exposure-meter flux rather than to any individual order, so that the global open-shutter interval is determined consistently before order-specific timing quantities are calculated. This serves two purposes. First, it avoids using bins dominated by shutter transitions or low-counts, which would instill a bias in the determination of exposure midpoints. Second, it provides a check on the actual illuminated portion of the exposure, rather than assuming that the interval is described perfectly by the header values alone. Exposures with fewer than five valid open bins are rejected, since such cases do not contain enough reliable information for robust timing and barycentric analysis.

2.1.2 Exposure Timing Verification and Correction

Accurate timing is fundamental to precise barycentric corrections, as errors in exposure midpoint times propagate directly to radial velocity errors [8]. Once the open-shutter bins are identified, the pipeline gathers a corrected start and end time for the exposure. The first and last bins above threshold generally correspond to partial shutter opening and closing, so they do not represent fully illuminated bins. To account for this, we use the measured flux in the first and last open bins together with the mean flux in the stable interior portion of the exposure to estimate when the shutter was effectively fully open and fully closed.

Let f_1 and f_N denote the fluxes in the first and last bins with substantial flux, and let $\langle f \rangle$ denote the mean flux in the intermediate bins for which the shutter is fully open. If the exposure-meter cadence is Δt, then the shutter-open and shutter-close times are estimated as

$$t_{\text{open}} = t_1 - \Delta t \left(\frac{f_1}{\langle f \rangle} - \frac{1}{2} \right), \tag{2.1}$$

and

$$t_{\text{close}} = t_N + \Delta t \left(\frac{f_N}{\langle f \rangle} - \frac{1}{2} \right), \tag{2.2}$$

where t_1 and t_N are the centers of the first and final time bins with substantial flux. These expressions estimate the fraction of each edge bin that was effectively illuminated.

From here the pipeline derives the effective exposure duration, the offset between the corrected and header-based start times, the offset between the corrected and header-based end times, and the shutter asymmetry between opening and closing delays. These quantities are stored for each exposure and provide a way to assess whether the header timing is a good description of the actual photon arrival time.

The uncertainty in the shutter-open and shutter-close times follows from the uncertainties in the edge-bin fluxes and in the estimate of the mean fully open flux, where $\sigma_{\langle f \rangle} \approx \sigma_f / \sqrt{N}$. For $N \gg 1$, the second term is negligible and we obtain

$$\sigma_{o/c} = \Delta t \frac{\sigma_f}{\langle f \rangle}, \tag{2.3}$$

and for the total measured exposure time $t_{\text{exp}} = t_{\text{close}} - t_{\text{open}}$,

$$\sigma_{t_{\text{exp}}} = \sqrt{2}\, \Delta t \frac{\sigma_f}{\langle f \rangle}. \tag{2.4}$$

2.1.3 Geometric and Flux-Weighted Midpoint Times

After the open interval is established, the pipeline computes two distinct representative times for each spectral order. The first is the geometric midpoint time (GMPT), defined simply as the start time of the exposure plus half the exposure duration:

$$t_{\text{GMPT}} = t_{\text{start}} + \frac{t_{\text{exp}}}{2}$$

where t_{start} is the shutter-open time and t_{exp} is the total exposure duration. This is the standard approximation used when no flux-weighted timing information is available.

The second is the flux-weighted midpoint time (FWMPT), defined as

$$t_{\text{FWMPT}} = \frac{\sum_i t_i F_i}{\sum_i F_i}$$

where t_i is the time of the ith exposure-meter bin and F_i is the flux measured in that bin for the order under consideration. The uncertainty in flux-weighted midpoint times under the assumption of constant uncertainty in each time bin. For this derivation, we ignore the subtlety that the first and final time bins include shutter opening and closing, as this does not materially affect the approximation when $N \gg 1$. Under normal conditions, all f_i values when the shutter is open are similar, and we approximate that they all have the same uncertainty σ_f.

$$\sigma_\tau \approx \frac{\sigma_f}{\dot{f}} \sqrt{\frac{T \Delta t}{3}}, \tag{2.5}$$

where $\dot{f}$ is the typical flux rate.

To verify our timing methodology, both GMPT and FWMPT were computed from scratch using only the exposure-meter flux and time data, then compared to the header values reported by the NEID pipeline. Across multiple exposures, the difference was taken between the computed geometric midpoint and the header midpoint time, confirming that our implementation correctly recovers the reported timing.

The GMPT is the natural midpoint one would adopt if the exposure were treated purely geometrically, with all photons assumed to be equally representative of the observation. The FWMPT, by contrast, is the temporal centroid of the detected photons and therefore reflects the actual time weighting of the observation. If the incoming flux were constant throughout the exposure, these two times would coincide. In practice they differ because the flux varies in time, and that variation can differ from order to order because the atmosphere attenuates different wavelengths differently. This distinction is the core of the chromatic barycentric problem. Since the barycentric correction is time dependent, a wavelength-dependent shift in the effective midpoint implies a wavelength-dependent barycentric correction.

2.1.4 Barycentric Velocity Calculation with `barycorrpy`

With verified timing information, barycentric corrections are computed using `barycorrpy` [11], which implements the formalism of [8] and is designed for barycentric-correction precision at the cm s^{-1} level. The calculations are performed separately for GMPT and FWMPT in order to quantify the systematic differences introduced by chromatic atmospheric effects.

Parameter	**Value**
Right Ascension (α)	`QRA` from header
Declination (δ)	`QDEC` from header
Proper motion in RA (μ_α)	-1729.726 mas yr^{-1}
Proper motion in DEC (μ_δ)	855.493 mas yr^{-1}
Parallax (π)	277.5162 mas
Radial velocity (v_r)	-16.597 km s^{-1}
Epoch	2457206.375 (J2015.5)

Table 2.1: Astrometric parameters used for barycentric correction calculations on Tau Ceti with `barycorrpy`. Celestial coordinates are extracted directly from NEID FITS headers.

In the current implementation, the pipeline uses the NEID header quantities `QRA`, `QDEC`, `QPMRA`, `QPMDEC`, `QPLX`, and `QRV`, converting proper motions from as yr^{-1} to mas yr^{-1} and radial velocity from km s^{-1} to m s^{-1}. The epoch adopted is J2015.5, corresponding to a Julian date of 2457206.375, and all barycentric calculations use the DE430 planetary ephemeris.

For each of the 122 exposure-meter orders, the pipeline extracts the order-specific flux time series over the valid open bins and computes both t_{FWMPT} and t_{GMPT}. Orders with zero summed flux over the open interval are excluded. The representative times are then converted to absolute UTC timestamps by adding the measured offsets to the header value of `DATE-OBS`. These quantities are first computed in km s^{-1} and seconds, respectively, and the barycentric velocity differences are then converted to $\mathrm{cm\,s}^{-1}$ to place them directly on the scale relevant for extreme-precision radial velocity work. And this order-by-order approach is essential. If one were to compute only a single midpoint for the entire exposure, one would lose the chromatic information that is the focus of the present study.

The primary products of the analysis are the wavelength-dependent barycentric correction difference,

$$\Delta\mathrm{BC}(\lambda) \equiv \mathrm{BC}_{\mathrm{GMPT}} - \mathrm{BC}_{\mathrm{FWMPT}}(\lambda)$$

expressed in $\mathrm{cm\ s}^{-1}$, and the corresponding timing offset,

$$\Delta t(\lambda) \equiv t_{\mathrm{FWMPT}}(\lambda) - t_{\mathrm{GMPT}}$$

expressed in seconds. These quantities are then modeled and compared across many exposures in order to characterize the magnitude and structure of the chromatic barycentric effect in NEID data.

2.1.5 Polynomial Modeling of Chromatic Dependence

The smooth wavelength dependence of the chromatic barycentric effect can be summarized by fitting a third-order polynomial [10] to the filtered values of $\Delta\mathrm{BC}(\lambda)$:

$$\Delta\mathrm{BC}(\lambda) \approx a_3\lambda^3 + a_2\lambda^2 + a_1\lambda + a_0. \tag{2.6}$$

This polynomial is not a physical atmospheric model, and should certainly not be seen as such. Rather, it acts as a compact representation of the smoothly varying chromatic structure seen across the optical spectrum. A simple cubic was chosen as it is flexible enough to capture curvature across the full wavelength range while remaining simple enough to avoid over-fitting any noise.

Across the exposures shown, a clear wavelength dependence is visible in the barycentric correction difference $\Delta\mathrm{BC}(\lambda)$. At shorter wavelengths, near ~ 400 nm, the chromatic effect is present but relatively modest, and the geometric midpoint and flux-weighted midpoint produce barycentric corrections that differ only slightly. In this region the exposure meter still improves the determination of the effective observation time, but the correction is comparatively small.

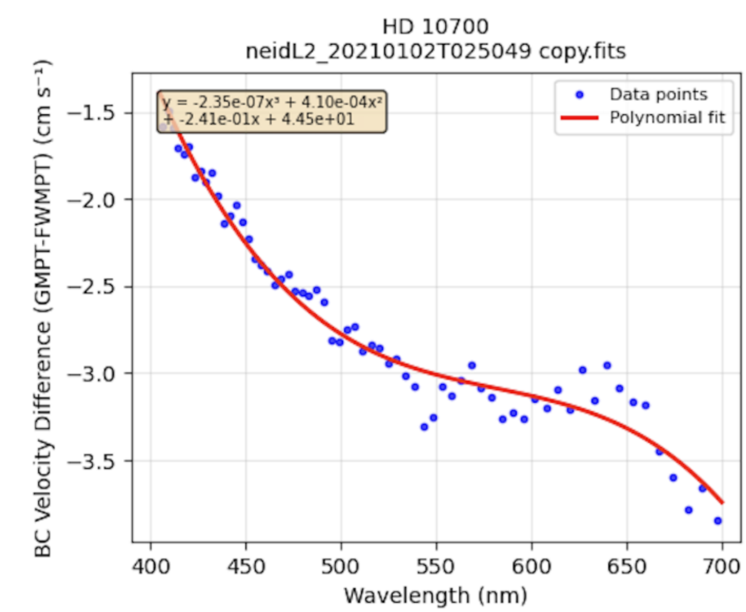

Figure 2.1: An example Tau Ceti exposure from 2021. Across $400 - 700$ nm, $\Delta\mathrm{BC}(\lambda)$ varies by approximately $2\ \mathrm{cm\,s^{-1}}$. The red end of the spectrum shows systematically larger differences, indicating stronger chromatic effects at longer wavelengths.

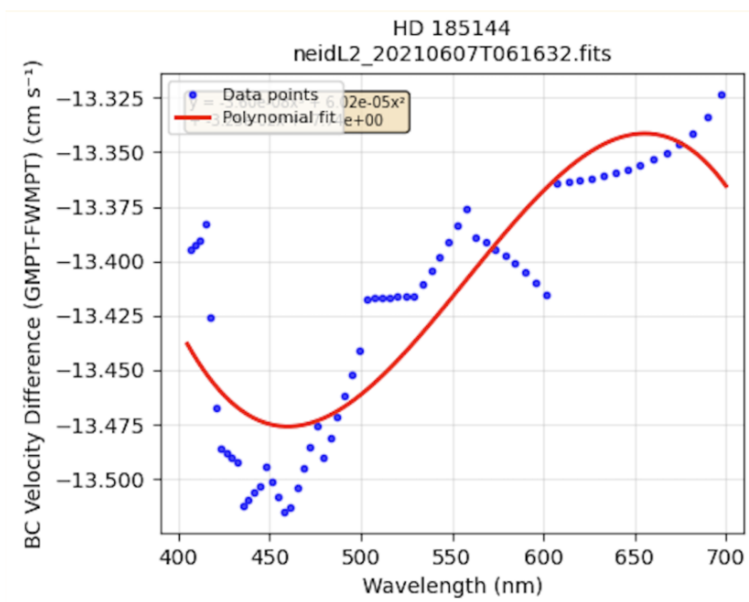

Figure 2.2: Example exposure of Sigma Draconis showing a small chromatic barycentric effect. The range of $\Delta\mathrm{BC}(\lambda)$ across the optical bandpass was approximately $0.175\ \mathrm{cm\,s^{-1}}$, indicating that the chromatic exposure meter was less critical on this night compared to nights with larger atmospheric variability.

Towards longer wavelengths, however, particularly near ~ 700 nm, the chromatic behavior becomes more pronounced. In every exposure examined here, the red orders show a systematic divergence between GMPT and FWMPT barycentric corrections. This indicates that the photon arrival times in the red portion of the spectrum are more strongly affected by variations in atmospheric transmission. For each exposure, the fitted polynomial and its coefficients are stored together with metadata describing the retained wavelength range, the number of valid orders, and the number of filtered data points. The total span of the fitted chromatic correction is also recorded through the minimum and maximum values of the filtered $\Delta\mathrm{BC}(\lambda)$ array.

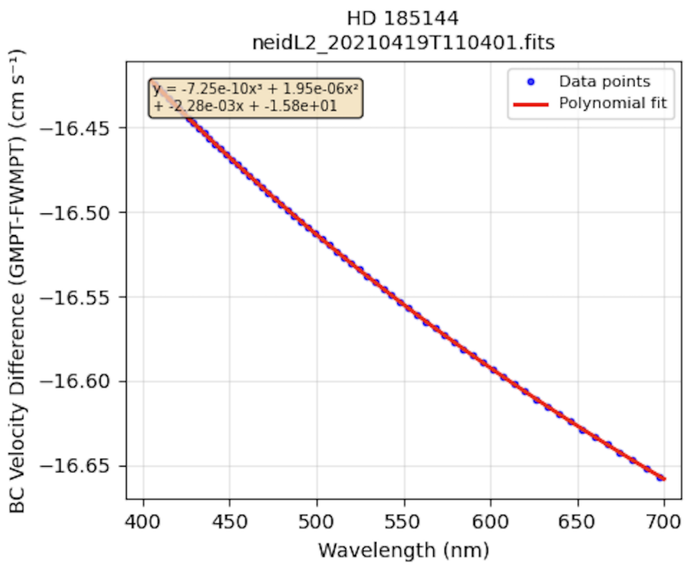

Figure 2.3: Several exposures exhibited an unusually good fit to the cubic polynomial, with residuals near zero. The cause of this behavior is unclear and may warrant further investigation

2.1.6 Residual Analysis and Goodness-of-Fit Metrics

For each exposure, the quality of the polynomial representation is quantified by comparing the measured values of $\Delta\mathrm{BC}(\lambda)$ to the fitted model evaluated at the same wavelengths. The residuals are defined as

$$r_i = \Delta\mathrm{BC}(\lambda_i) - P(\lambda_i), \tag{2.7}$$

where $P(\lambda)$ is the best-fit cubic polynomial. From these residuals, the pipeline computes the root-mean-square error,

$$\mathrm{RMSE} = \sqrt{\frac{1}{N}\sum_{i=1}^{N} r_i^2}, \tag{2.8}$$

along with the mean residual, residual standard deviation, maximum absolute residual, and the coefficient of determination R^2.

These metrics quantify how well a smooth polynomial describes the chromatic barycentric structure within a given exposure. Small RMSE and large R^2 values indicate that the wavelength dependence is smooth and well captured by the adopted low-order model, whereas larger residuals suggest increased noise.

2.1.7 Exposure-Level Summary Statistics

Beyond the polynomial fit itself, we derive several exposure-level summary quantities intended to characterize the practical significance of the chromatic barycentric effect. The most important of these is the total range of the filtered barycentric correction difference,

$$\mathrm{Range}\big[\Delta\mathrm{BC}(\lambda)\big] = \max\big(\Delta\mathrm{BC}\big) - \min\big(\Delta\mathrm{BC}\big), \tag{2.9}$$

which provides a simple measure of the amplitude of the wavelength-dependent barycentric correction across the optical range.

The pipeline also computes the mean timing offset,

$$\langle \Delta t \rangle = \frac{1}{N}\sum_{i=1}^{N} \Delta t(\lambda_i), \tag{2.10}$$

and its absolute value. In the interpretation adopted here, the range of $\Delta\mathrm{BC}(\lambda)$ acts as a measure of the importance of the chromatic barycentric effect, while $|\langle \Delta t \rangle|$ is used as an operational proxy for the degree to which time-asymmetric photon weighting shifts the photon-weighted temporal centroid away from the geometric midpoint.

2.1.8 Multi-Exposure Comparison and Identification of Extreme Cases

After processing all exposures in a target set, it computes overall summary statistics for the RMSE and R^2 distributions, identifying the exposures with the largest and smallest ranges in $\Delta\mathrm{BC}(\lambda)$, and generates the plots for extreme cases. It also tabulates the distribution of the chromatic range across the sample using summary quantities such as the mean, median, extrema, and selected percentiles.

The amplitude of the chromatic barycentric correction can be quantified using the range of $\Delta\mathrm{BC}(\lambda)$ across the optical bandpass. In the exposures analyzed here, the observed ranges are typically on the order of several centimeters per second, with the largest cases approaching roughly ~ 15 cm,s^{-1}. Even in these extreme cases, the chromatic range measured for NEID remains smaller than the amplitudes reported for instruments such as EXPRES, reflecting differences in instrument design and ADC [10].

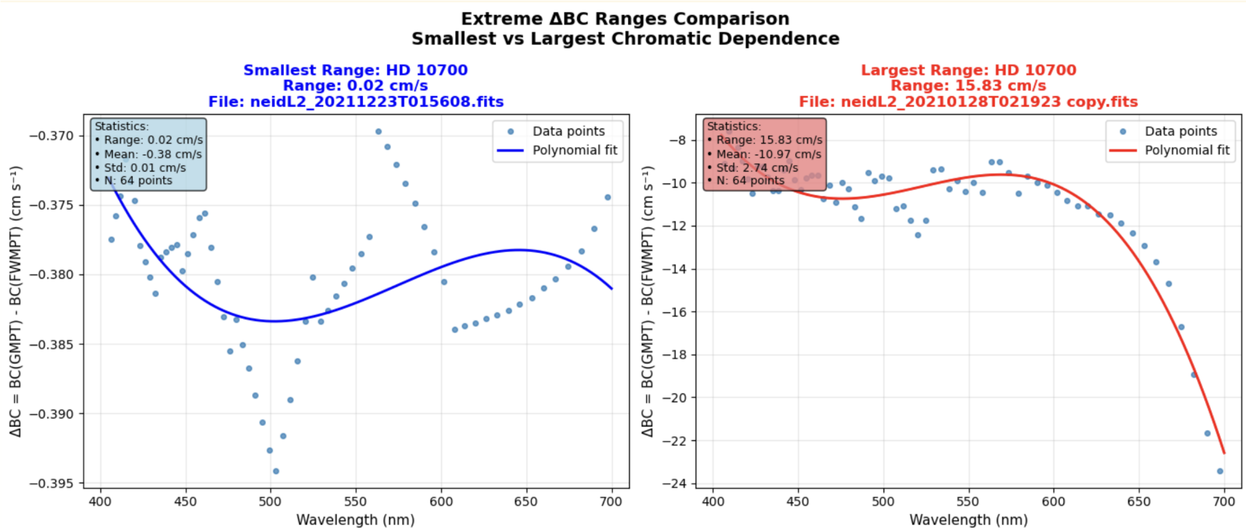

Figure 2.4: Extreme cases for Tau Ceti exposures. The contrast is striking and highlights the variance between exposures. The smallest range (left) shows that although still useful, the exposure meter was less necessary compared to the large range (right), where $\Delta\mathrm{BC}(\lambda)$ varied by $\sim 15\ \mathrm{cm\ s^{-1}}$.

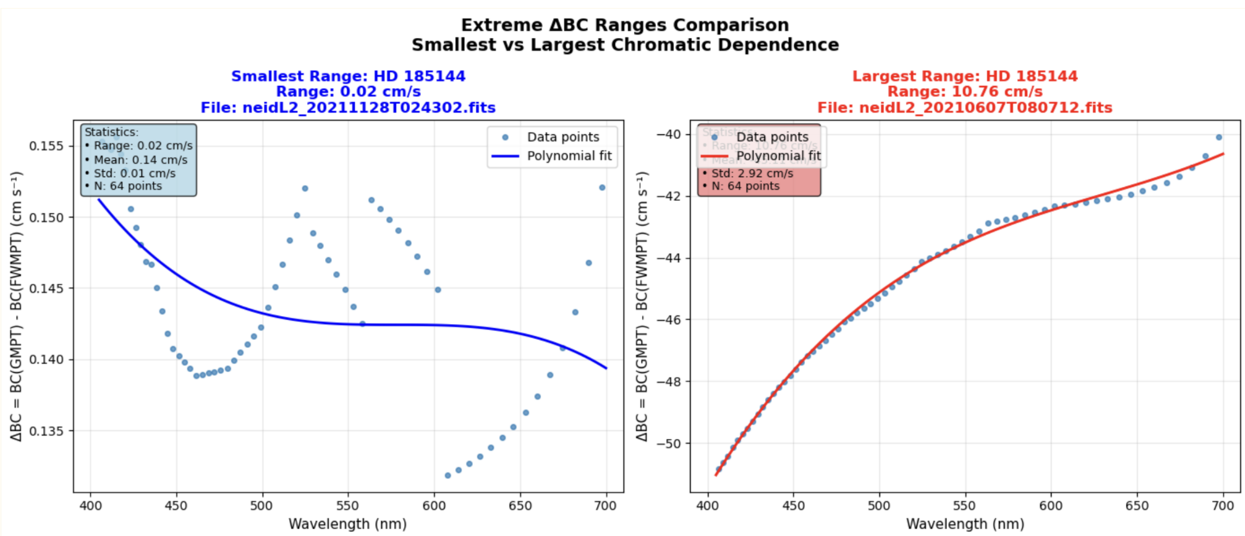

Figure 2.5: Both extremes for Sigma Draconis. The smaller $\Delta\mathrm{BC}(\lambda)$ (left) is again contrasted with the larger $\Delta\mathrm{BC}(\lambda)$ (right) of $\sim 10\ \mathrm{cm\ s^{-1}}$, a clear and visual validation of the chromatic exposure meter.

A separate comparison is performed between the exposure-level range of $\Delta\mathrm{BC}(\lambda)$ and the absolute mean timing offset $|\langle\Delta t\rangle|$. This comparison is used to test whether larger departures between FWMPT and GMPT tend to be associated with larger chromatic barycentric amplitudes. Although this does not provide a direct physical model of atmospheric conditions, it offers an empirical way to relate the magnitude of timing asymmetry to the significance of the resulting wavelength-dependent barycentric correction.

Taken together, these steps produce a complete characterization of chromatic barycentric effects in the NEID exposures analyzed here: from raw time-resolved exposure-meter fluxes, to order-by-order effective timing, to wavelength-dependent barycentric correction differences, to statistical summaries of their magnitude and smoothness. The methodology is therefore designed not merely to compute simple barycentric corrections, but to evaluate whether a chromatic, exposure-meter-informed treatment is necessary for NEID observations at a precision relevant to modern exoplanet radial velocity work.

Chapter 3

Conclusion

3.1 The Analysis So Far

3.1.1 Discussion

Here, we have investigated the wavelength dependence of barycentric corrections in NEID observations by comparing geometric midpoint times and flux-weighted midpoint times derived from the exposure meter—by validating the pipeline products and quantifying the BC uncertainty. By analyzing the exposure-meter flux order by order with `barycorrpy`, and modeling the resulting $\Delta\mathrm{BC}(\lambda)$ structure across the optical spectrum, this work quantified the extent to which chromatic photon weighting alters the appropriate barycentric correction. The results demonstrate that, for an extreme-precision radial velocity instrument such as NEID, the effective time of observation cannot be described by a single geometric midpoint and must instead be understood as a wavelength-dependent quantity.

A central strength of NEID for this problem is that its exposure meter preserves wavelength-dependent flux information in a way that allows the temporal weighting of photons to be examined across spectral orders. This makes NEID a particularly potent instrument for investigating chromatic barycentric effects at the precision level relevant to modern exoplanet radial velocity surveys. In this sense, the present work serves both as a verification of the importance of exposure-meter-informed timing and as an implementation of chromatic barycentric correction analysis in the specific instrumental context of NEID. We resolve that NEID's methods, likely attributable to the ADC, surpass the precision on EXPRES.

More broadly, this thesis establishes a practical framework for quantifying wavelength-dependent barycentric effects using exposure-meter data. As radial velocity instrumentation pushes toward the detection of Earth-mass planets in the habitable zones of Sun-like stars, effects that once seemed secondary will become dominant within an increasingly shrinking error budget. By characterizing how chromatic weighting modifies barycentric corrections, this work contributes to ensuring that future radial velocity precision is limited by astrophysical signals rather than by uncorrected instrumental or atmospheric systematics.

3.1.2 Future Work

The next stage is to simulate a standard white-light spectrograph with no exposure meter, for which only a single integrated exposure time is available, and an instrument that possesses an exposure meter but lacks the wavelength-dependent weighting in NEID through its ADC design. These comparisons will allow us to evaluate how strongly the fidelity of the exposure-meter system influences the accuracy of the chromatic correction, directly assessing the advantage of NEID's more informative timing architecture. An investigation of the role air mass may play on wavelength will also be undertaken, and an investigation of the wavelength-dependent weights themselves to quantify the impact of chromatic weighting on the final barycentric correction is already underway.

If the difference between geometric and flux-weighted timing proves negligible for simpler systems, then a white-light midpoint approximation may be sufficient in some observing regimes. If, however, NEID's wavelength-resolved timing information substantially reduces systematic barycentric errors relative to these other approaches, this would provide strong evidence that chromatic exposure-meter weighting is an essential feature for future instruments aiming at the cm s^{-1} level.

This is unlikely, however, and will almost certainly prove as a demonstration—a litmus test of sorts—as to the importance of NEID's chromatic exposure meter

Future work will also expand beyond the bright, benchmark targets used here. Extending the pipeline to a larger and more diverse set of stars will permit us to determine whether the magnitude and shape of $\Delta\mathrm{BC}(\lambda)$ varies systematically across different kinds of targets and observing conditions. Such an expanded sample will strengthen the statistical basis for comparing NEID to other spectrograph architectures and for evaluating when chromatic barycentric corrections are required in extreme-precision radial velocity observations.

Bibliography

[1] Michel Mayor and Didier Queloz. A Jupiter-mass companion to a solar-type star. , 378(6555):355–359, November 1995.

[2] Imke de Pater and Jack J. Lissauer. *Planetary Sciences*. 2015.

[3] Jason T. Wright. Precise radial velocities. In Nikku Madhusudhan, editor, *ExoFrontiers: Big Questions in Exoplanet Science*, pages 5–1–5–24. IOP Publishing, 2020.

[4] Gregory W. Henry, Geoffrey W. Marcy, R. Paul Butler, and Steven S. Vogt. A Transiting "51 Peg-like" Planet. , 529(1):L41–L44, January 2000.

[5] S. Udry, X. Bonfils, X. Delfosse, T. Forveille, M. Mayor, C. Perrier, F. Bouchy, C. Lovis, F. Pepe, D. Queloz, and J.-L. Bertaux. The HARPS search for southern extra-solar planets. XI. Super-Earths (5 and 8 M$\{\oplus\}$) in a 3-planet system. , 469(3):L43–L47, July 2007.

[6] Guillem Anglada-Escudé, Pedro J. Amado, John Barnes, Zaira M. Berdiñas, R. Paul Butler, Gavin A. L. Coleman, Ignacio de La Cueva, Stefan Dreizler, Michael Endl, Benjamin Giesers, Sandra V. Jeffers, James S. Jenkins, Hugh R. A. Jones, Marcin Kiraga, Martin Kürster, María J. López-González, Christopher J. Marvin, Nicolás Morales, Julien Morin, Richard P. Nelson, José L. Ortiz, Aviv Ofir, Sijme-Jan Paardekooper, Ansgar Reiners, Eloy Rodríguez, Cristina Rodríguez-López, Luis F. Sarmiento, John P. Strachan, Yiannis Tsapras, Mikko Tuomi, and Mathias Zechmeister. A terrestrial planet candidate in a temperate orbit around Proxima Centauri. , 536(7617):437–440, August 2016.

[7] Debra A. Fischer, Guillem Anglada-Escude, Pamela Arriagada, Roman V. Baluev, Jacob L. Bean, Francois Bouchy, Lars A. Buchhave, Thorsten Carroll, Abhijit Chakraborty, Justin R. Crepp, Rebekah I. Dawson, Scott A. Diddams, Xavier Dumusque, Jason D. Eastman, Michael Endl, Pedro Figueira, Eric B. Ford, Daniel Foreman-Mackey, Paul Fournier, Gabor Fűrész, B. Scott Gaudi, Philip C. Gregory, Frank Grundahl, Artie P. Hatzes, Guillaume Hébrard, Enrique Herrero, David W. Hogg, Andrew W. Howard, John A. Johnson, Paul Jorden, Colby A. Jurgenson, David W. Latham, Greg Laughlin, Thomas J. Loredo, Christophe Lovis, Suvrath Mahadevan, Tyler M. McCracken, Francesco Pepe, Mario Perez, David F. Phillips, Peter P. Plavchan, Lisa Prato, Andreas Quirrenbach, Ansgar Reiners, Paul Robertson, Nuno C. Santos, David Sawyer, Damien Segransan, Alessandro Sozzetti, Tilo Steinmetz, Andrew Szentgyorgyi, Stéphane Udry, Jeff A. Valenti, Sharon X. Wang, Robert A. Wittenmyer, and Jason T. Wright. State of the Field: Extreme Precision Radial Velocities. , 128(964):066001, June 2016.

[8] Jason T. Wright and Jason D. Eastman. Barycentric corrections at 1 cm s^{-1} for precise radial velocities. *Publications of the Astronomical Society of the Pacific*, 126(943):838, 2014.

[9] Ryan T. Blackman, Andrew E. Szymkowiak, Debra A. Fischer, and Colby A. Jurgenson. Chromatic barycentric corrections for exoplanet detection and characterization. *The Astrophysical Journal*, 837(1):18, 2017.

[10] Ryan T. Blackman, J. M. Joel Ong, and Debra A. Fischer. The measured impact of chromatic atmospheric effects on barycentric corrections: Results from the extreme precision spectrograph. *The Astrophysical Journal*, 883(2):170, 2019.

[11] Shubham Kanodia and Jason Wright. Barycorrpy: A python package for precision barycentric corrections. *Research Notes of the American Astronomical Society*, 2(1):4, 2018.